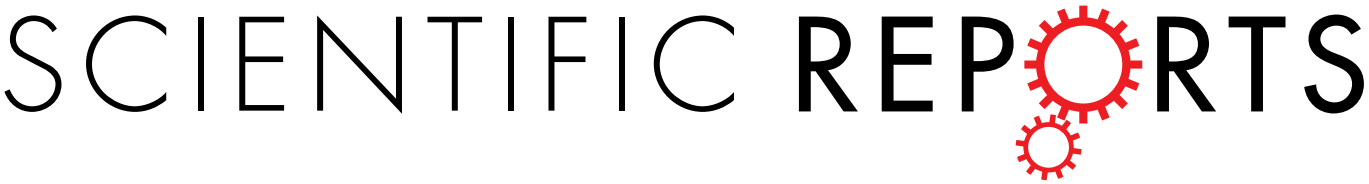

OPEN

On the impact of Vertical Alignment of MoS_2 for Efficient Lithium Storage

Received: 9 February 2017
Accepted: 4 May 2017
Published online: 12 June 2017

Victor Shokhen[1], Yana Miroshnikov[1], Gregory Gershinsky[1], Noam Gotlib[2], Chen Stern[2], Doron Naveh[2] & David Zitoun[1]

Herein, we report energy storage devices, which are based on densely packed, vertically aligned MoS_2 (VA-MoS_2) or planar oriented MoS_2 (PO-MoS_2) and compare their electrochemical performances. The VA-MoS_2 films have been processed by chemical vapor deposition (CVD) to reach unprecedented micron-scale thick films while maintaining the vertical alignment for the whole thickness. The VA-MoS_2 and the PO-MoS_2 films form a high-performance Li-ion electrode, reaching the theoretical limits of reversible capacity for this material (800 mAh/g; twice the specific capacity of graphite). The vertical alignment allows faster charge-discharge rates while maintaining a high specific capacity (C-rate measurements). Noteworthy, the reversible cycling of the Li-ion electrode also benefits from the vertical alignment. In this article, we present the full synthesis, structural and electrochemical characterization of VA-MoS_2 along with the properties of PO-MoS_2 to deconvolute the intrinsic properties of MoS_2 from the influence of the layers' orientation.

Materials such as graphite and layered transition-metal disulfides (LTMDs) are structured from 2D sheets, stacked together by Van der Waals interactions. These rather weak interactions enable the exfoliation of stable two-dimensional sheets by mechanical methods[1–3] chemical methods[4,5] and ultrasonic agitation processing in solution[6,7]. Apart from the exfoliation methods, growth of ultrathin layered materials by chemical vapor deposition (CVD) has been successfully demonstrated on graphene[8,9], hexagonal boron nitride h-BN[10], molybdenum disulfide (MoS_2)[11], tungsten diselenide (WSe_2)[12] and more[13,14]. CVD has been established as an efficient method for the preparation of large crystals with high quality and controllable thickness[15,16], together with ALD[17]. In most cases, CVD growth yields 2D materials with basal planes oriented parallel to the substrate, with planar orientation (PO)[18]. This orientation is preferred for the study of the electronic properties of the layers and for the implementation of electronic devices[19]. In particular, the majority of the extensive studies on MoS_2 growth strive to achieve continuous layers and heterostructures with PO suitable for electronic and optoelectronic devices[20–22]. Layered materials, MoS_2 in particular, have also been demonstrated as efficient and promising for energy storage applications[23–25], where the weak interlayer force can accommodate intercalated ions very efficiently. However, for energy storage, the most efficient orientation of MoS_2 crystals is the vertical alignment (VA) to the substrate, and the desired thickness of the grown layer must be sufficient to insert as many ions as possible, intercalated between the MoS_2 crystal planes.

CVD has previously led to very thin films of VA-MoS_2 (5–25 nm) by sulfurization of thin Mo films[26–28]. The transition from PO to VA growth has been rationalized through the investigation of the Mo layer thickness. Above a certain Mo thickness (3 nm), the preferential growth in vertically aligned has been reported for no more than 25 nm thick MoS_2[29]. VA-MoS_2 has shown stable electrocatalytic activity for the hydrogen evolution reaction (HER)[28,30,31]. However, the intriguing question of its performance as an ion-storing device remains unanswered.

The interaction of alkaline cations in MoS_2 has been studied from several perspectives, including several device geometries and electrode designs, as well as the choice of cations to be hosted within the electrode. Li-ion batteries are the most used energy source for devices[32–35]. The lithium storage in LTMDs was found to follow a mechanism similar to that of graphite[36], but with higher specific capacity[23] at a higher and safer potential[37–39]. The relation of the material geometry and dimensionality to its lithium storage capacity has been extensively

[1]Department of Chemistry, Bar Ilan Institute of Nanotechnology and Advanced Materials (BINA), Bar Ilan University, Ramat Gan, 5290002, Israel. [2]Faculty of Engineering, Bar Ilan Institute of Nanotechnology and Advanced Materials (BINA), Bar Ilan University, Ramat Gan, 5290002, Israel. Correspondence and requests for materials should be addressed to D.N. (email: Doron.Naveh@biu.ac.il) or D.Z. (email: David.Zitoun@biu.ac.il)

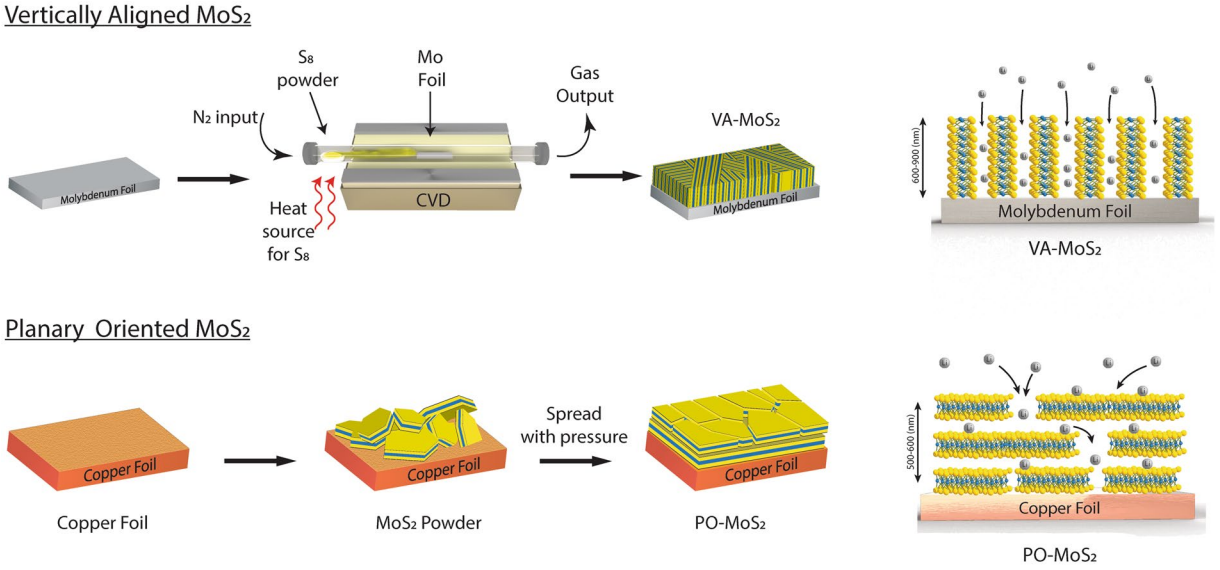

Figure 1. Scheme of the chemical vapor deposition (CVD) experimental set-up and the VA-MoS_2 electrodes, scheme of the preparation of PO-MoS_2 electrodes and expected lithiation pathways.

studied[40–43]. Exfoliated materials, either graphene or LTMD monolayers[44,45], demonstrate very high capacity although we do not fully understand their electrochemical mechanisms[46]. Interestingly, the same processes of intercalation can be used for the preparation of exfoliated LTMDs[23]. MoS_2 flakes have been tested as Li-ion electrodes with the reversible capacity of 200 mA/g when cycled in the electrochemical window of 1–3 V vs. Li/Li^+ [47], which matches the intercalation of one Li atom per formula[48]. Such an intercalation can theoretically occur for most of the cations[49]. In contrast, MoS_2 nanoflakes cycled in a wider potential window of 0.01–3 V show a high reversible capacity of 840 mA/g, corresponding to more than 5 Li/MoS_2[50], which does not match the intercalation mechanism, but a full conversion reaction to Li_2S and Mo[51]. Furthermore, nanocomposite MoS_2 or graphene show a high discrepancy between the reported reversible capacities in the range of 650–1,500 mAh/g in the electrochemical window of 0–3 V[39,52,53]. More generally, the literature does not provide a fully consistent report on the properties of MoS_2 by itself and on the influence of the crystal orientation on the lithiation properties.

Here, for the first time, we study the performance of Li-storage devices comprised of VA-MoS_2 and compare the measured capacitance and energy density to those achieved with PO-MoS_2. For the synthesis of VA-MoS_2, we use a simple Mo foil compatible with the lithium storage. The sulfurization of Mo into a highly ordered thick layer of VA-MoS_2 was achieved by a long reaction time. The comparison to PO-MoS_2 was conducted on films of similar thickness in order to isolate the dependence on crystal orientation from the influence of film thickness on the overall performance of the electrodes.

Results

Synthesis. The synthesis of the VA-MoS_2 was carried out by placing polished molybdenum foil in the CVD furnace (Fig. 1). The sample was purged by nitrogen gas in a thermal annealing step followed by the growth of a MoS_2 film. During the process, sulfur vapor was introduced into the furnace from a boat filled with sulfur. The reaction was carried out for different durations, leading to several film thicknesses. Henceforth, we refer to the samples of thicknesses 900 nm, 800 nm and 560 nm as VA-MoS_2 #1, VA-MoS_2 #2 and VA-MoS_2 #3, respectively. After the reaction, the foil changed color from silver to dark purple (Fig. S1 in the Supplementary Information). The film thickness was measured by atomic profile analysis through Rutherford backscattering spectroscopy (RBS) (Fig. S2).

Structural characterization. A slice of VA-MoS_2 #1 was cut by a focused ion beam (FIB) and the cross-section was imaged and analyzed by high resolution transmission electron microscopy (HRTEM) in a bright field. (Figure 2A), The HRTEM shows the polycrystalline nature of the Mo foil marks as a light blue line and the green line marks the MoS_2 grown from the surface of the Mo foil and a layer of Pt (added during the FIB process for the purpose of the experiment). VA-MoS_2 #1 displays a homogeneous thickness of 900 nm throughout the sample.

Interestingly, the MoS_2 film displays vertically aligned grain boundaries (Fig. 2B), which arise from the vertical orientation of the film grown from the surface of the Mo foil (Fig. 2A and B). The HRTEM analysis and fast-Fourier transform (FFT) image (Fig. 2C and inset) show lattice fringes of 6.3 Å, corresponding to the (002) basal planes of the 2H-MoS_2 phase, confirming the vertical alignment of the film. The basal planes were found to be orthogonal to the substrates on all the HRTEM images, showing growth along the (100) plane parallel to the substrate. The almost-perfect VA of the MoS_2 stabs from the top to the bottom can be clearly observed (Fig. 2D), while a close view shows the abrupt interface between the Mo foil and the MoS_2 film (Fig. 3A). In some cases, MoS_2 basal planes grow parallel to the Mo foil close to the interface while, in general the vertical growth starts

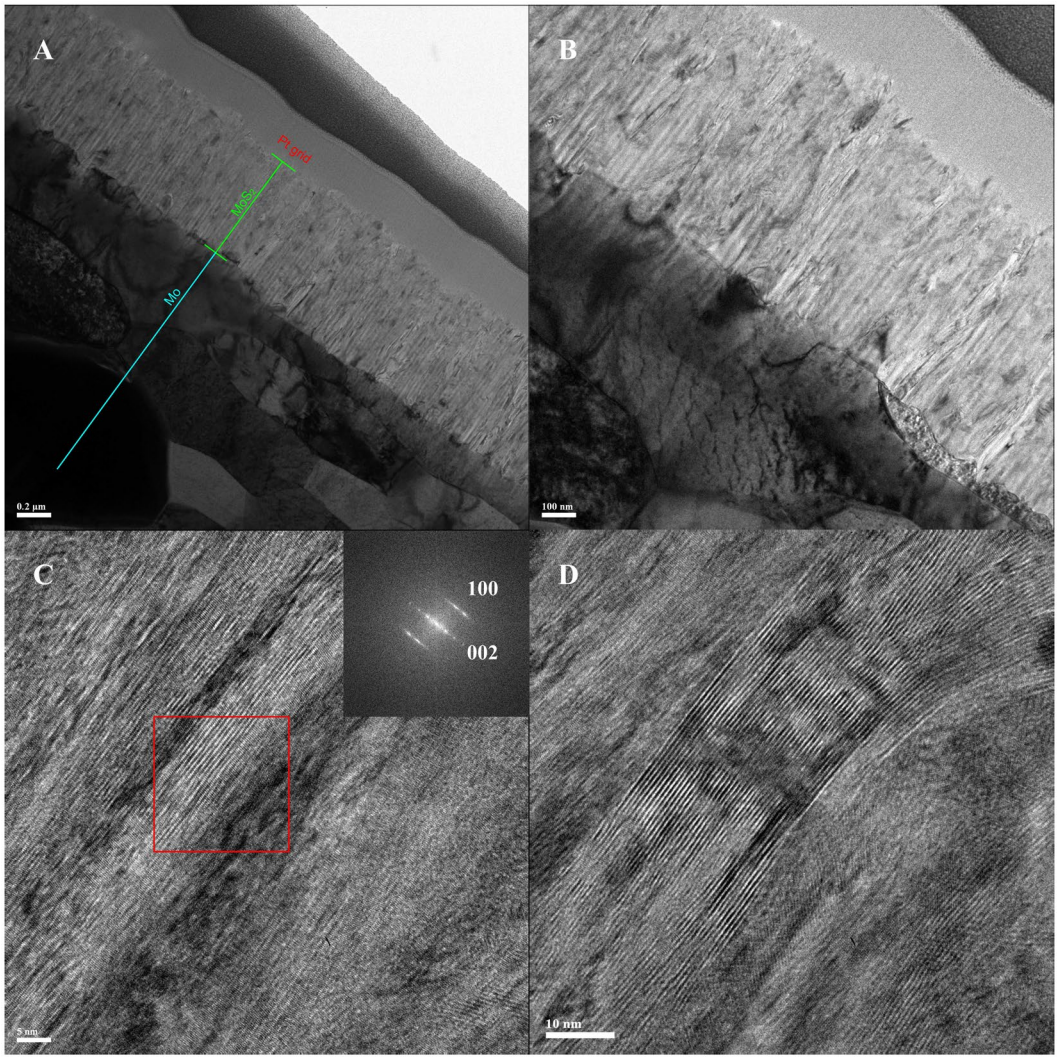

Figure 2. Transmission electron microscopy (TEM) images of VA-MoS_2 #1 grown on Mo foil with different magnifications (**A**,**B**); high resolution TEM (HRTEM) of several areas and FFT from the selected red square (**C**,**D** and inset).

directly from the interface. On the surface of the film, the layered MoS_2 opens in a flower-like morphology with a roughness on the order of several nanometers (Fig. 3B).

The high quality of the film is confirmed by SEM (Fig. 4A–D) on the whole sample. The roughness surface morphology of VA-MoS_2 #1 is measured by atomic force microscopy (AFM) (Fig. 4E,F). The pristine Mo foil was polished before synthesis. After synthesis, the surface displays randomly oriented vertical flakes, which is consistent with the polycrystalline nature of the film. The roughness reaches the mean value of 21.4 nm.

The crystalline orientation of the film should impact the lithium intercalation. MoS_2 flakes with micron-scale thickness (comparable to the CVD-grown samples) display a planar orientation (PO) while laminated on roughened copper foil used as a current collector for the Li-ion battery (LIB). MoS_2 flakes on Cu were imaged on a scanning electronic microscope (Fig. S3). The "in-plane" images show the homogeneous layer of MoS_2 flakes (Fig. S3A and B), whereas the cross-section shows the PO of the flakes (Fig. S3C and D). The film is formed from a single layer of flakes 500 nm thick with a good adhesion to the current collector. The orientation of the film is confirmed by Raman spectroscopy which displays the typical in-plane Mo−S phonon mode (E^1_{2g}) and the out-of-plane Mo-S phonon mode (A^1_g) (Fig. S4). The A_{1g} to E_g ratio is close to 1:2 ratio for the PO-MoS_2[25] while the VA-MoS_2 displays a 1:3 ratio revealing the edge terminated nature of the film, i.e. the vertical alignment[28]. The same MoS_2 flakes were also formulated in a slurry with a binder and carbon additive. The addition of a polymer and carbon black yields a thicker film with random orientation of the flakes.

X-ray diffraction (XRD) was carried out on VA-MoS_2, PO-MoS_2 and randomly oriented MoS_2 flakes in the slurry (Fig. 5). Bragg-Brentano (θ–2θ) XRD of the MoS_2 slurry exclusively shows the reflections assigned to the 2H-MoS_2 phase (ICCD #00-037-1492) together with the reflections of the copper foil underneath (Fig. 5A). In the case of PO-MoS_2 flakes on Cu foil, the XRD only displays the reflections from the basal planes (002), a clear sign of the preferential orientation of the flakes parallel to the Cu foil. In contrast, the CVD-grown sample lacks the

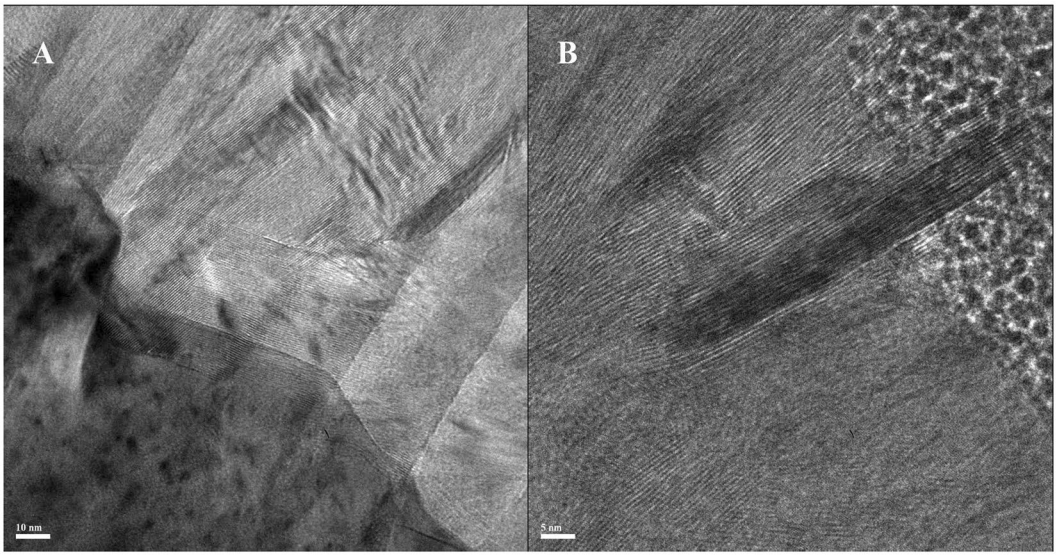

Figure 3. HRTEM of the bottom of the VA-MoS_2 #1 at the interface with Mo (**A**) and HRTEM of the top of the film (**B**).

(002) reflection and shows two main reflections: (100) of the 2H-MoS_2 and (200) of the Mo foil. The XRD pattern confirms the orientation growth observed in HRTEM with vertically aligned basal planes and a growth along the (100) direction. Grazing incidence XRD (GIXRD) on the CVD-grown samples allows focusing on the MoS_2 film itself, without the Mo background (Fig. 5B).

Electrochemical characterization. All the electrodes were tested for Li storage under similar conditions with MoS_2 as the working electrode and lithium as the counter-electrode and reference electrodes in a coin cell with a glassy paper separator impregnated with an EC/DMC 1 M $LiPF_6$ electrolyte (see Experimental Section). Figure 6 displays the cyclic voltammograms (CV) over the range of 0.01–3.0 V versus Li/Li^+. During the first cycle, VA-MoS_2 #1 shows lithiation at 1.1 and 0.55 V and delithiation at 2.25 V (Fig. 6A). In the following cycles, the low potential peaks fade and the main lithiation-delithiation occurs between 2.2 and 1.8 V. This behavior points to the formation of a surface-electrolyte interphase (SEI) during the first cycle, followed by reversible intercalation processes in the following cycles. MoS_2 flakes show similar behavior with slightly lower values for the lithiation potentials and higher values for the delithiation ones at the same scanning rate, revealing more sluggish kinetics (Fig. 6B). On the VA-MoS_2 #1 sample, the potential was narrowed to 1.5 to 3.0 V after a few stabilizing cycles and the same faradic peaks as in the wide potential window are observed (Fig. 6C). Interestingly, the faradic peaks correspond to the electrochemistry of sulfur and not the intercalation of Li in MoS_2. Therefore, most of the faradic capacity in the material can be obtained on a narrower potential window.

The galvanostatic measurements on the samples are measured at a C/3 rate (3 hours charge and discharge) for at least 100 cycles for all samples (Fig. 7). The specific capacity of VA-MoS_2, PO-MoS_2 and MoS_2 slurry is compared. Binder-free MoS_2 (VA and PO) perform far better than the slurry, whose capacity rapidly fades from an initial 500 mAh/g value (Fig. 7A). Binder-free MoS_2 displays a stable specific capacity of more than 700 mAh/g with a tendency to fade after 65 cycles for the PO-MoS_2. The VA-MoS_2 does not show any fading after 100 cycles and its specific capacity reaches 750 mAh/g. The different CVD-grown samples display almost the same specific capacity within a statistical error bar (Fig. 7B). The only observable discrepancy (a higher initial capacity for VA-MoS_2 #3) arises from different conditioning of the cell which has not gone through CV measurements. These high specific capacities cannot be explained by a simple intercalation mechanism since it would involve only one lithium atom per MoS_2 unit (~200 mAh/g). A specific capacity of 670 mAh/g corresponds to four lithium atoms. The potential of the vertically aligned sample displays two plateaus at 1.2 and 0.6 V for the first discharge (Fig. 7C, black curve). The first lithiation matches the intercalation of one Li atom in MoS_2 and the second plateau corresponds to the insertion of three Li atoms. However, the second insertion does not correspond to an intercalation process but probably to conversion towards the Mo and Li_2S phases. After 100 cycles, the specific capacity is retained but the voltage profile is smoother. Similar behavior is observed for PO-MoS_2, which indicates that the insertion mechanism does not vary with the crystallographic orientation.

Figure 8 displays the Coulombic efficiency for each of the LIBs. The VA sample reaches values of 98% Coulombic efficiency, much higher than the PO flakes (94–96%) (Fig. 8A). The values are low compared to the acceptable standards in LIBs since the electrodes consist of thin films. Nevertheless, the comparison between the Coulombic efficiencies shows the benefits of the CVD growth regardless of film thickness (Fig. 8B). Figure 8C reveals the kinetics of the lithium insertion during a C-rate experiment. The current density gradually increases and then decreases for a corresponding charge duration of 1 hour and, finally, 3 min. It is interesting to note that the insertion kinetics for the CVD-grown samples is not improved, despite the vertical alignment which favors the Li intercalation between the basal planes.

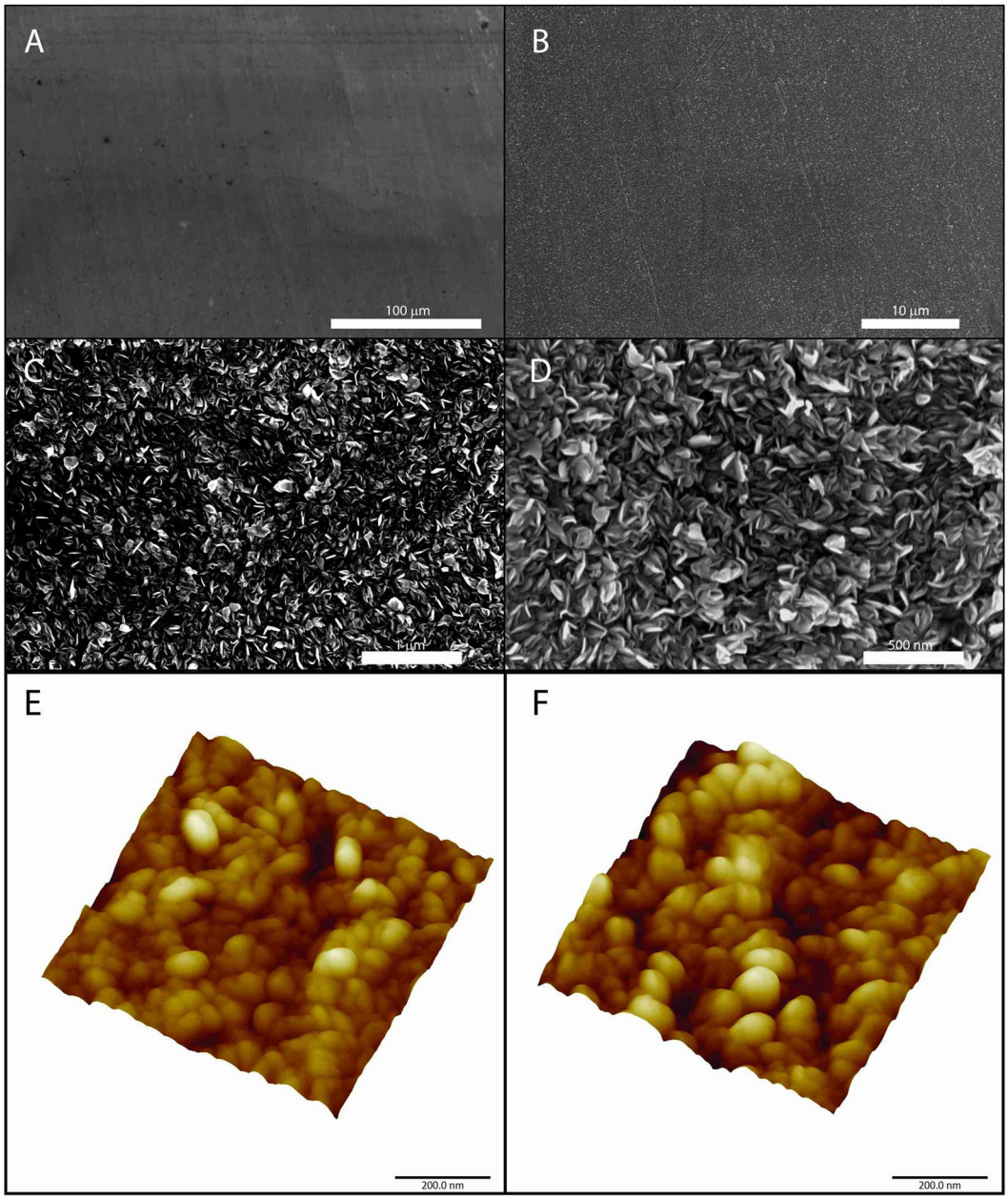

Figure 4. Scanning electron microscopy (SEM) (**A**–**D**) and atomic-force microscopy of VA-MoS_2 #1 (**E**,**F**).

To further demonstrate this point, electrochemical impedance spectroscopy (EIS) has been carried out on the batteries during 30 cycles. The typical Nyquist plots of the VA-MoS_2 #1 and PO-MoS_2 are shown in Fig. 8D after 10 cycles, at 3 V. For each EIS spectrum, two regions can be clearly seen: the semi-circle region corresponds to the charge transfer resistance at high frequency; the linear region (Warburg) corresponds to the Li-ion diffusion into the active material. The VA and PO electrodes shows similar charge-transfer resistance, indicating fast and highly efficient faradaic reactions for the two electrodes. The vertical alignment shows a slight enhancement of the Li-ion diffusion in the Warburg region with a higher slope compared to the planar orientation.

Furthermore, the post-mortem SEM analysis of the electrodes demonstrate that the vertical alignment remains even after multiple cycles (Fig. 9). The flakes of VA- MoS_2 #1 after 10 cycles do have a preferred orientation even if the lithiation delithiation processes induce some disorder and a loose packing. A similar behavior has been observed on the PO-MoS2 which display a planar orientation of the flakes after 10 cycles as shown in supporting information (Fig. S6).

Discussion

CVD growth of vertically aligned VA-MoS_2 has been previously demonstrated on very thin samples. In the present study, the process is applied to much thicker films and VA 2H-MoS_2 is grown with a thickness ranging between 500 and 1,000 nm. The layers are perfectly aligned and grow along the (100) orientation from the Mo

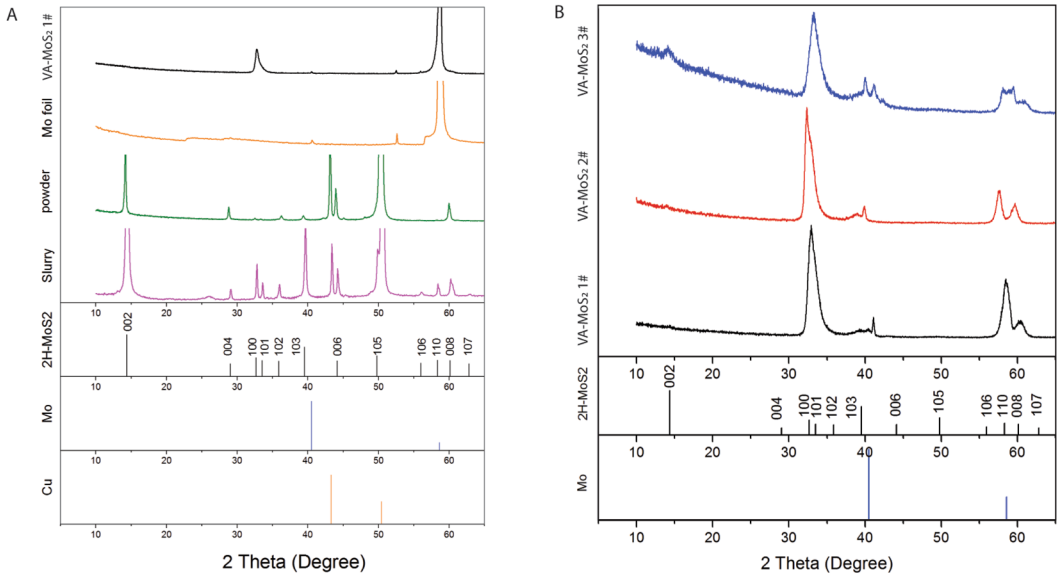

Figure 5. X-Ray diffraction (XRD) patterns of MoS_2 films in slurry on Cu, PO-MoS_2 on Cu and VA-MoS_2 #1 on Mo (**A**); Grazing incidence-XRD (GIXRD) of CVD-grown samples (**B**).

foil, which itself has a preferential (200) orientation. However, no direct correlation can be drawn from the lattice parameters and we cannot claim epitaxial growth.

The electrochemistry of LTMDs has recently been extensively studied in exfoliated systems. In most of the publications, the authors correlate the high specific capacities to the low dimensionality of the materials. Nevertheless, metal sulfides, whether in the form of layered materials or not, have been studied in the bulk form and show a two-step lithiation mechanism. Goodenough *et al*. brought evidence from galvanostatic cycling and crystallographic data in favor of an intercalation process followed by the conversion of the materials towards metal and Li_2S[48]. *This conversion mechanism is clearly verified quantitatively in our study where the specific capacity reaches the theoretical limit of 800 mAh/g, with a 1 to 3 ratio between the two lithium insertions, corresponding to the formation of* $LiMoS_2$ *by intercalation and* $Mo + Li_2S$ *by conversion* (Fig. 7E,F).

The high specific capacity obtained in a wide potential window (0–3 V is not of practical use as an electrode material) is retained in a narrower window (1.5–3 V), with most of the capacity at about 2 V. The conversion reaction turns out to be an alloying mechanism involving sulfur as the electroactive material. Elemental sulfur is the most promising element for future development of high-energy cathodes. Recent research papers have shown that the combination of LTMDs, namely, MoS_2 with elemental sulfur, displays excellent stability even after hundreds of cycles[49]. The role of Mo has yet to be fully understood but the outcomes of our findings underline a generic concept for any LTMD. The demonstration of the full theoretical specific capacity in VA-MoS_2 paves the way to high energy devices based on VA-LTMDs.

In comparison, the thin PO-MoS_2 films also show a high specific capacity reaching the same theoretical value, but the specific capacity cannot be sustained more than 70 cycles. The main benefits arising from vertical alignment are the higher stability in cycling and Coulombic efficiency. Since the samples display similar thickness, the orientation must be responsible for the discrepancies. All the VA samples show better performance than the PO ones although the differences are not as extensive as one could have predicted. This assessment is obvious from analyzing the first electrochemical process, the intercalation of Li between the basal planes of MoS_2 being very similar for the two orientations (Fig. 7C,D). In the conversion process that follows, the relationship between the structure and the conversion reaction is far more elusive and would require in-depth operando experiments to probe the electrode structure during cycling. Our preliminary results from EIS and post-morten SEM show that the cycling tends to conserve the film orientation. The VA alignment benefits to the Li ion diffusion and explains the differences observed between the two different orientations. These results are consistent with other materials grown as nano-walls and used as electrodes for LIBs.

In summary, CVD-grown VA-MoS_2 films show a high reversible capacity of 800 mAh/g versus lithium, which corresponds to the theoretical limit of MoS_2. The specific capacity is stable for more than 100 cycles at C/3 rate and reveals the full conversion to Mo and Li_2S. The CVD process is developed to grow 2H-MoS_2 films hundreds of nanometers thick with vertically aligned (VA) stacking directly from the Mo foil. The film shows large domains of perfectly aligned basal planes of 2H-MoS_2 orthogonal to the foil. Noteworthy, both binder free MoS_2 electrodes, planary oriented or vertically aligned, show high reversible capacity and the advantages of the vertical alignment become obvious while comparing with randomly oriented MoS_2 electrodes with binder. Comparing the binder free electrodes, the VA electrodes show better capacity retention than their PO counterparts, which fail after 70 cycles and the vertical alignment allows faster charge-discharge rates while maintaining a high specific capacity (C-rate measurements). Apart from their interesting electrochemical properties, the CVD of dense and thick VA-LTMD films pave the way towards high performance energy storage devices.

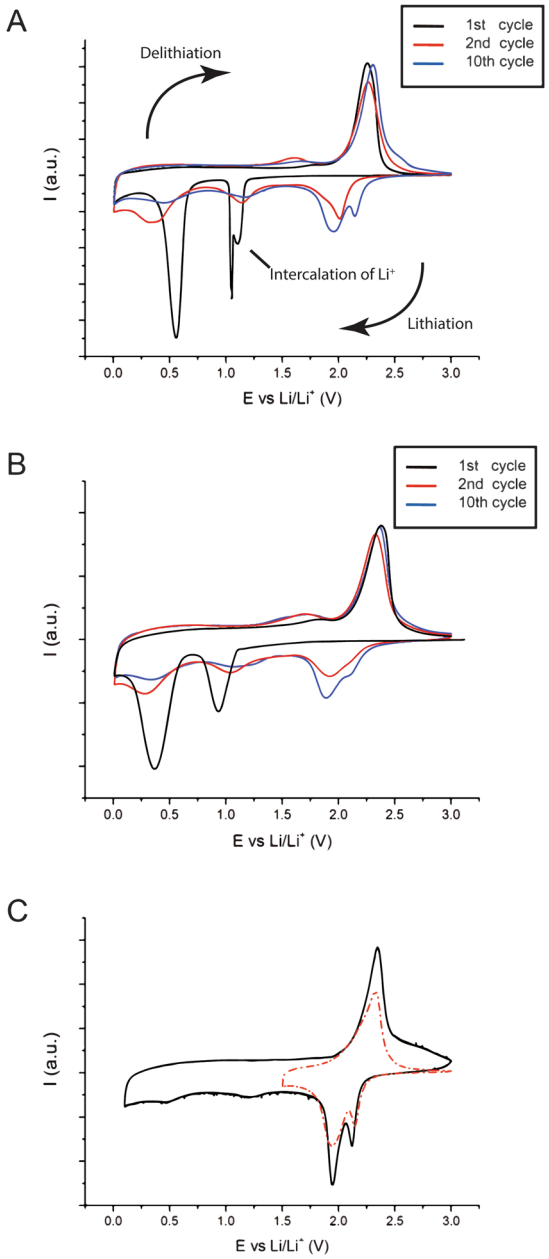

Figure 6. Cyclic voltammograms (1, 2 and 10) at 0.1 mV/s versus Li metal of VA-MoS_2 #1 (**A**) and PO-MoS_2 (**B**); cyclic voltammograms (50) of VA-MoS_2 #1 in wide (black line) and narrow (red line) potential window (**C**).

Methods

VA-MoS_2 synthesis. Molybdenum foil (0.05 mm thick, 99.95%, STREM) was polished and carefully washed. The polishing of the foil to a surface roughness of 21 nm was achieved with 50-nm alumina (see Supplementary Information), followed by cleaning with acetone, iso-propanol and 2 M HCl. The Mo pieces were introduced into a one-inch quartz tube. Sulfur (Sigma-Aldrich CAS #7704-34-9) was introduced into a boat in a different heat zone. The furnace was cleared of gas until a base pressure of Torr was reached, and then purged with nitrogen at 100 sccm for 10 minutes. Mo was then heated to 500 °C and S was heated to 145 °C. A temperature of 750 °C was maintained for 24, 48 or 72 hours and then the sulfur was cooled down to ambient temperature. The Mo foil was then cooled for over 2 hours.

Electrode preparation. VA-MoS_2 was used without further treatment by cutting disks from the foil. MoS_2 powder (Sigma-Aldrich, $<2\,\mu m$, 99%) was laminated onto a roughened copper foil (Oxygenfree, SE-Cu58, Schlenk Metallfolien GmbH & Co. KG) to yield PO-MoS_2. The powder was brushed evenly over the surface (binder-free electrode: PO-MoS2). The slurry was made with 70% MoS_2 powder (Sigma-Aldrich, $<2\,\mu m$, 99%), 10% carbon black and 20% polyvinylidene fluoride (PVDF) from N-methyl pyrrolidone (NMP). The slurry was stirred overnight and then spread with a hand coater (wire rod diameter of 0.05 mm) on the Cu foil.

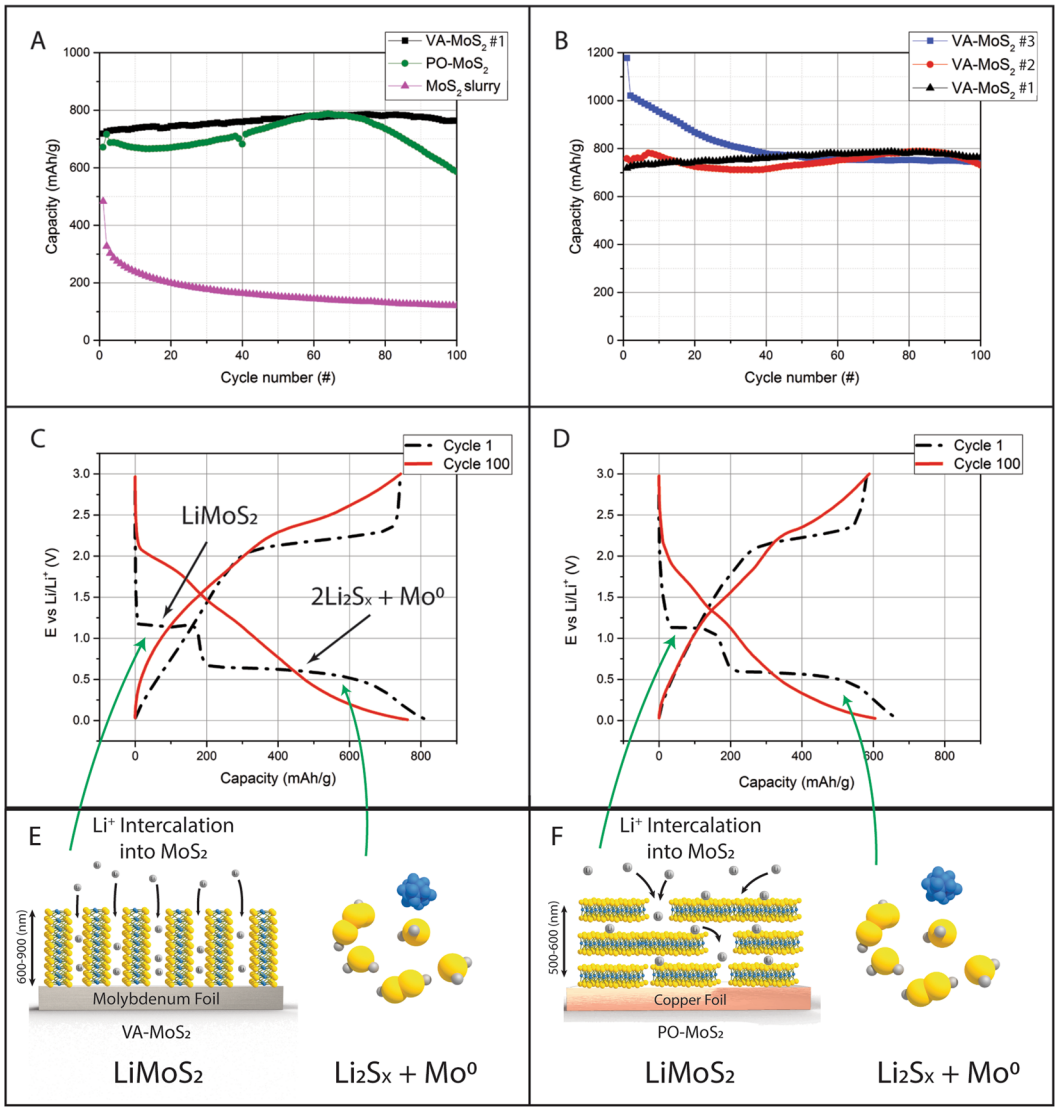

Figure 7. Specific capacity from galvanostatic measurements at a C/3 rate of VA-MoS_2 #1, PO-MoS_2 and slurry electrodes (**A**); Specific capacity at a C/3 rate of VA-MoS_2 #1 (black triangle), VA-MoS_2 #2 (red dots) and VA-MoS_2 #3 (blue squares); voltage profile of cycle 1 (black dotted line) and cycle 100 (red plain line) for VA-MoS_2 #1 (**C**) and PO-MoS_2 (**D**); lithiation mechanism in VA-MoS_2 (**E**) and PO-MoS_2 (**F**).

Characterization. A focused ion beam (FIB) (FEI, Helios 600) was used to cut the CVD grown samples into lamellas for transmission electron microscopy (TEM) observation. High-resolution TEM (HRTEM) images were obtained by a JEOL JEM-2100 (LaB6) operated at 200 kV. Atomic force microscopy (AFM) measurements were carried out using a Bio FastScan scanning probe microscope (Bruker AXS). All images were obtained using the tapping mode with a FastScan-A (Bruker) silicon probe (spring constant of 18 N/m). For image processing and surface roughness analysis, the Nanoscope Analysis Software was used. Rutherford backscattering spectroscopy (RBS) was performed using a 1.7 M V Pelletron accelerator from NEC. RBS and particle-induced x-ray emission (PIXE) spectra were acquired simultaneously. The PIXE data were analyzed using the GUPIX software. Raman spectroscopy was carried out on Horiba LabRam HR evolution with a 532 nm Laser.

X-ray diffraction (XRD) images were collected on a Rigaku Smartlab XRD in Bragg-Brentano (θ–2θ) and grazing-incidence XRD (GIXRD) mode. For the GIXRD, grazing-incidence parallel beam optics (PB/PSA) with a fixed incident angle of 0.8° was used. The X-ray generator was operated at 40 kV and 30 mA with Cu-Kα radiation ($\lambda = 1.54$ Å). Scanning electron microscopy (SEM) images were collected on a FEI Quanta FEG250 on the pristine electrodes and after washing with dry dimethyl carbonate and drying on the cycles electrodes.

Electrochemistry. The electrodes were tested in coin-type cells (2523, NRC, Canada) vs. lithium metal (Chemetall Foote Corporation, USA) using glassy paper (Hollingsworth & Vose, BGM03010). The electrolyte solution was ethylene carbonate/dimethyl carbonate (EC/DMC) (1/1 ratio) with 1 M LiPF6 (purelyte, Ube

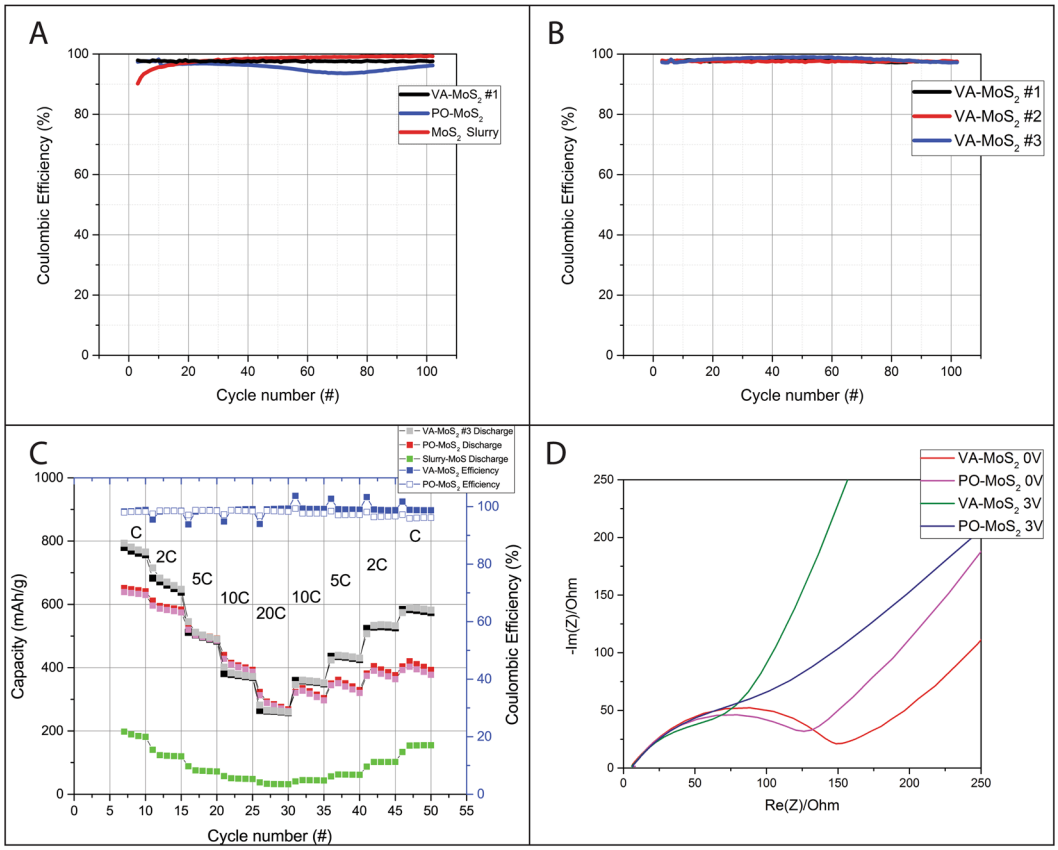

Figure 8. Coulombic efficiency at C rate of VA-MoS_2 #1 (black), PO-MoS_2 (red) and slurry (blue) (**A**); Coulombic efficiency at C rate of VA-MoS_2 #1 (black), VA-MoS_2 #2 (red) and VA-MoS_2 #3 (blue) (**B**); C-rate of VA-MoS_2 #1 (black), PO-MoS_2 (red) and slurry (green) with the corresponding coulombic efficiency for VA-MoS_2 #1 (blue); Nyquist plots of the VA-MoS_2 #1 and PO-MoS_2 after 10 cycles at 0 V and 3 V vs Li metal (**D**).

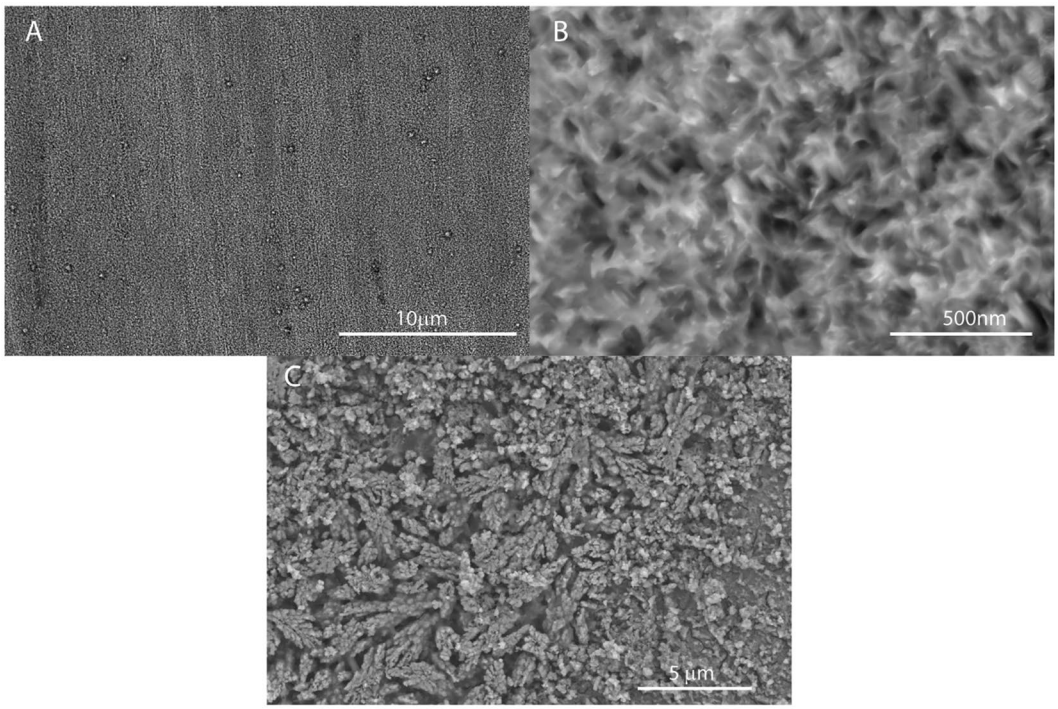

Figure 9. Scanning electron microscopy (SEM) of VA-MoS_2 #1 after 10 cycles.

industries). The cells were assembled in an argon-filled glovebox with a purifying system (MBraun GmbH, Germany) (Fig. S5).

Cyclic voltammetry was performed with a Bio-Logic VMP3 multi-channel potentiostat at 0.1 mV/s between 0.01–3.0 V and 1.5–3.0 V vs. Li^+/Li with EIS. The coin-cells were cycled at 30 °C using an Arbin MSTAT BT2000 battery cycler at a C/3 rate, and the C rate was tested under the same conditions after 100 cycles.

References

1. Ferrari, A. C. & Basko, D. M. Studying the properties of graphene. *Nature* **8**, 235–246 (2013).
2. Novoselov, K. S. *et al*. REVIEW A roadmap for graphene. *Nature* **490**, 192–200 (2012).
3. Butler, S. Z. *et al*. Opportunities in Two-Dimensional Materials Beyond Graphene. *ACS Nano* **7**, 2898–2926 (2013).
4. Jeong, S., Yoo, D., Ahn, M. & Miro, P. conventional exfoliation processes. *Nat. Commun.* **6**, 5763 (2015).
5. Hu, L., Ren, Y., Yang, H. & Xu, Q. Fabrication of 3D Hierarchical MoS2/Polyaniline and MoS2/C Architectures for Lithium-Ion Battery Applications. *ACS Appl. Mater. Interfaces* **6**, 14644–14652 (2014).
6. Bernal, M. M. & Milano, D. In *Carbon Nanotechnology* 159–185 (2014).
7. Kim, J. *et al*. materials in pure water via temperature control. *Nat. Commun.* **6**, 8294 (2015).
8. Fang, W., Hsu, A. L. & Kong, J. A review of large-area bilayer graphene synthesis by chemical vapor deposition. *Nanoscale* **7**, 20335–20351 (2015).
9. Volder, M. F. L. D., Tawfick, S. H., Baughman, R. H. & Hart, A. J. Carbon Nanotubes: Present and Future Commercial Applications. *Science* **339**, 535–539 (2013).
10. Jang, S. K., Youn, J., Song, Y. J. & Lee, S. Synthesis and Characterization of Hexagonal Boron Nitride as a Gate Dielectric. *Sci. Rep.* **6**, 30449 (2016).
11. Jeon, J. *et al*. Layer-controlled CVD growth of large-area two-dimensional MoS_2 films. *Nanoscale* **7**, 1688–1695 (2015).
12. Liu, B., Fathi, M., Chen, L., Abbas, A. & Zhou, C. Chemical Vapor Deposition Growth of Monolayer WSe2 with Tunable Device Characteristics and Growth. *ACS Nano* **9**, 6119–6127 (2015).
13. Tan, C. & Zhang, H. Two-dimensional transition metal dichalcogenide nanosheet-based composites. *Chem. Soc. Rev.* **44**, 2713–2731 (2015).
14. Shi, Y. & Li, L. Chem Soc Rev Recent advances in controlled synthesis of two- dimensional transition metal dichalcogenides via. *Chem. Soc. Rev.* **44**, 2744–2756 (2015).
15. Zhan, Y., Liu, Z., Najmaei, S., Ajayan, P. M. & Lou, J. Large-area vapor-phase growth and characterization of MoS2 atomic layers on a SiO 2 substrate. *Small* **8**, 966–971 (2012).
16. Yu, Y. *et al*. Controlled Scalable Synthesis of. *Sci. Rep.* **3**, 1866–1871 (2013).
17. Tan, L. K. *et al*. Atomic layer deposition of a MoS_2 film. *Nanoscale* **6**, 10584–8 (2014).
18. Zhang, G., Liu, H., Qu, J. & Li, J. Two-Dimensional Layered MoS2: Rational Design, Properties and Electrochemical Applications. *Energy Environ. Sci.* **9**, 1190–1209 (2016).
19. Sørensen, S. G., Fu, H. G., Tuxen, A. K., Walton, A. S. & Lauritsen, J. V. Structure and Electronic Properties of *In Situ* Synthesized Single-Layer MoS2 on a Gold Surface. *ACS Nano* 6788–6796 (2014).
20. Amani, M. *et al*. High Luminescence Efficiency in MoS2 Grown by Chemical Vapor Deposition. *ACS Nano* **10**, 6535–6541 (2016).
21. Datta, K. & Khosru, Q. D. M. Electronic Properties of MoS2/MX2/MoS2 Trilayer Heterostructures: A First Principle Study. *ECS J. Solid State Sci. Technol.* **5**, 3001–3007 (2016).
22. Hong, X. *et al*. Ultrafast charge transfer in atomically thin MoS2/WS 2 heterostructures. *Nat. Nanotechnol.* **9**, 682–686 (2014).
23. Chhowalla, M. *et al*. The chemistry of two-dimensional layered transition metal dichalcogenide nanosheets. *Nat. Chem.* **5**, 263–275 (2013).
24. Pumera, M., Sofer, Z. & Ambrosi, A. Layered transition metal dichalcogenides for electrochemical energy generation and storage. *J. Mater. Chem. A* **2**, 8981–8987 (2014).
25. Kiriya, D. *et al*. General thermal texturization process of MoS2 for efficient electrocatalytic hydrogen evolution reaction. *Nano Lett.* **16**, 4047–4053 (2016).
26. Wang, H. *et al*. Electrochemical tuning of vertically aligned MoS2 nanofilms and its application in improving hydrogen evolution reaction. *Proc. Natl. Acad. Sci. USA* **110**, 19701–19706 (2013).
27. Gaur, A. P. S. *et al*. Optical and Vibrational Studies of Partially Edge-Terminated Vertically Aligned Nanocrystalline MoS2 Thin Films. *J. Phys. Chem. C* **117**, 26262–26268 (2013).
28. Kong, D. *et al*. Synthesis of MoS2 and MoSe2 Films with Vertically Aligned Layers. *Nano Lett.* **13**, 1341–1347 (2013).
29. Jung, Y. *et al*. Metal seed layer thickness-induced transition from vertical to horizontal growth of MoS2 and WS2. *Nano Lett.* **14**, 6842–6849 (2014).
30. Wang, H. *et al*. MoSe 2 and WSe 2 Nano fi lms with Vertically Aligned Molecular Layers on Curved and Rough Surfaces. *Nano Lett.* **13**, 3426–3433 (2013).
31. Kang, M.-A. *et al*. Large scale growth of vertically standing MoS2 flakes on 2D nanosheet using organic promoter. *2D Mater.* **4**, 25045 (2017).
32. Tarascon, J. M. & Armand, M. Issues and challenges facing rechargeable lithium batteries. *Nature* **414**, 359–367 (2001).
33. Xia, H. *et al*. 16.Facile synthesis of chain-like LiCoO2 nanowire arrays as three-dimensional cathode for microbatteries. *NPG Asia Mater.* **6**, e126 (2014).
34. Xia, Q. *et al*. Black mesoporous $Li_4Ti_5O_{12-\delta}$ nanowall arrays with improved rate performance as advanced 3D anodes for microbatteries. *J. Mater. Chem. A* **4**, 17543–17551 (2016).
35. Xia, H. *et al*. Self-standing porous LiMn2O4 nanowall arrays as promising cathodes for advanced 3D microbatteries and flexible lithium-ion batteries. *Nano Energy* **22**, 475–482 (2016).
36. Raccichini, R., Varzi, A., Passerini, S. & Scrosati, B. energy storage. *Nat Mater* **14**, 271–279 (2015).
37. Wang, Q. H., Kalantar-Zadeh, K., Kis, A., Coleman, J. N. & Strano, M. S. Electronics and optoelectronics of two-dimensional transition metal dichalcogenides. *Nat. Nanotechnol.* **7**, 699–712 (2012).
38. Seh, Z. W. *et al*. High-capacity lithium sulphide cathodes. *Nat. Commun.* **5**, 5017 (2014).
39. Sun, F. *et al*. Melamine-assisted one-pot synthesis of hierarchical nitrogen-doped carbon@MoS2 nanowalled core-shell microspheres and their enhanced Li-storage performances. *Nanoscale* **7**, 13043–13050 (2015).
40. Sen, U. K., Johari, P., Basu, S., Nayak, C. & Mitra, S. An experimental and computational study to molybdenum disul fi de †. *Nanoscale* **6**, 10243–10254 (2014).
41. Ambrosi, A., Sofer, Z. & Pumera, M. 2H → 1T phase transition and hydrogen evolution activity of MoS2, MoSe2, WS2 and WSe2 strongly depends on the MX2 composition. *Chem. Commun.* **51**, 8450–8453 (2015).
42. Fan, X. *et al*. Fast and E ffi cient Preparation of Exfoliated 2H MoS2 Nanosheets by Sonication-Assisted Lithium Intercalation and Infrared Laser-Induced 1T to 2H Phase Reversion. *Nano Lett.* **15**, 5956–5960 (2015).
43. Vangelista, S. *et al*. Large scale growth of vertically standing MoS2 flakes on 2D nanosheet using organic promoter.
44. Jing, Y., Ortiz-Quiles, E. O., Cabrera, C. R., Chen, Z. & Zhou, Z. Layer-by-layer hybrids of MoS2 and reduced graphene oxide for lithium ion batteries. *Electrochim. Acta* **147**, 392–400 (2014).

45. Yu, X. Y., Hu, H., Wang, Y., Chen, H. & Lou, X. W. D. Ultrathin MoS < inf > 2 < /inf > Nanosheets Supported on N-doped Carbon Nanoboxes with Enhanced Lithium Storage and Electrocatalytic Properties. *Angew. Chemie - Int.* ed. **54**, 7395–7398 (2015).
46. Wang, H., Feng, H. & Li, J. Graphene and graphene-like layered transition metal dichalcogenides in energy conversion and storage. *Small* **10**, 2165–2181 (2014).
47. Fang, X. *et al*. Lithium storage in commercial MoS2 in different potential ranges. *Electrochim. Acta* **81**, 155–160 (2012).
48. Hu, Z. *et al*. MoS2 with intercalation reaction as long-life anode material for Lithium ion batteries. *Inorg. Chem. Front.* **3**, 532–535 (2016).
49. Shuai, J. *et al*. Density functional theory study of Li, Na, and Mg intercalation and diffusion in MoS2 with controlled interlayer spacing. *Mater. Res. Express* **3**, 64001–64008 (2016).
50. Xiong, F. *et al*. Li Intercalation in MoS2: *In Situ* Observation of Its Dynamics and Tuning Optical and Electrical Properties. *Nano Lett.* **15**, 6777–6784 (2015).
51. Feng, C. *et al*. Synthesis of molybdenum disulfide (MoS2) for lithium ion battery applications. *Mater. Res. Bull.* **44**, 1811–1815 (2009).
52. Jiang, L. *et al*. Monolayer MoS2-Graphene Hybrid Aerogels with Controllable Porosity for Lithium-Ion Batteries with High Reversible Capacity. *ACS Appl. Mater. Interfaces* **8**, 2680–2687 (2016).
53. Guo, J., Zhu, H., Sun, Y., Tang, L. & Zhang, X. Boosting the lithium storage performance of MoS_2 with graphene quantum dots. *J. Mater. Chem. A* **4**, 4783–4789 (2016).

Acknowledgements

The authors acknowledge Dr Olga Girshevitz for her kind assistance with the AFM and RBS, Dr. Judith Grinblat for the HRTEM, Dr. Yafit Fleger for the FIB and Gili Cohen-Taguri for the GIXRD. The authors acknowledge the support from the Israel National Research for Electrochemical Propulsion 2 (INREP 2), the Israel Science Foundation (1055/15) and the Israeli Ministry of Science, Technology and Space (Israel-South Korea bilateral program). Y.M. thanks the Israeli Ministry of Science, Technology and Space for its financial support.

Author Contributions

Zitoun and Naveh have developed the concept. Shokhen has designed and conducted the experiments (synthesis, characterization and electrochemistry). The manuscript was written by Zitoun through contributions of all authors. Gershinsky developed and analyzed the electrochemical results. Miroshnikov provided training and assistance on the experiments. Gotlib and Stern performed the CVD growth and the Raman spectroscopy. All authors have given approval to the final version of the manuscript.

Additional Information

Supplementary information accompanies this paper at doi:10.1038/s41598-017-03453-x

Competing Interests: The authors declare that they have no competing interests.

Publisher's note: Springer Nature remains neutral with regard to jurisdictional claims in published maps and institutional affiliations.